Astronomy & Astrophysics manuscript no. disks
January 8, 2016

Observations and modelling of CO and [C I] in protoplanetary disks

First detections of [C I] and constraints on the carbon abundance

M. Kama[1], S. Bruderer[2], M. Carney[1], M. Hogerheijde[1], E.F. van Dishoeck[1], D. Fedele[2], A. Baryshev[3,4], W. Boland[1,5], R. Güsten[6], A. Aikutalp[4], Y. Choi[4], A. Endo[7], W. Frieswijk[1,8], A. Karska[2,9], P. Klaassen[1,10], E. Koumpia[4], L. Kristensen[1,11], S. Leurini[6], Z. Nagy[4,12], J.-P. Perez Beaupuits[6], C. Risacher[3,6], N. van der Marel[1], T.A. van Kempen[1], R.J. van Weeren[1,11], F. Wyrowski[6], and U.A. Yıldız[1,13]

[1] Leiden Observatory, P.O. Box 9513, NL-2300 RA, Leiden, The Netherlands, e-mail: mkama@strw.leidenuniv.nl
[2] Max Planck Institut für Extraterrestrische Physik, Giessenbachstrasse 1, 85748 Garching, Germany
[3] SRON Netherlands Institute for Space Research
[4] Kapteyn Astronomical Institute, P.O. Box 800, 9700 AV Groningen, The Netherlands
[5] NOVA, J.H. Oort Building, P.O. Box 9513, 2300 RA Leiden, The Netherlands
[6] Max-Planck-Institut für Radioastronomie, Auf dem Hügel 69, 53121, Bonn, Germany
[7] Kavli Institute of Nanoscience, Delft University of Technology, Lorentzweg 1, 2628 CJ Delft, The Netherlands
[8] ASTRON, the Netherlands Institute for Radio Astronomy, Postbus 2, 7990 AA, Dwingeloo, The Netherlands
[9] Astronomical Observatory Institute, Faculty of Physics, A. Mickiewicz University, Sloneczna 36, 60-286, Poznan, Poland
[10] UK Astronomy Technology Center, Royal Observatory Edinburgh, Blackford Hill, Edinburgh EH9 3HJ, UK
[11] Harvard-Smithsonian Center for Astrophysics, 60 Garden Street, Cambridge, MA 02138, USA
[12] Department of Physics and Astronomy, University of Toledo, 2801 West Bancroft Street, Toledo, OH 43606, USA
[13] Jet Propulsion Laboratory, California Institute of Technology, 4800 Oak Grove Drive, Pasadena, CA 91109, USA

ABSTRACT

Context. The gas-solid budget of carbon in protoplanetary disks is related to the composition of the cores and atmospheres of the planets forming in them. The key gas-phase carbon carriers CO, C^0 and C^+ can now be observed regularly in disks.
Aims. The gas-phase carbon abundance in disks has thus far not been well characterized observationally. We aim to obtain new constraints on the [C]/[H] ratio in a large sample of disks, and to compile an overview of the strength of [C I] and warm CO emission.
Methods. We carried out a survey of the CO 6–5 and [C I] 1–0 and 2–1 lines towards 37 disks with the APEX telescope, and supplemented it with [C II] data from the literature. The data are interpreted using a grid of models produced with the DALI disk code. We also investigate how well the gas-phase carbon abundance can be determined in light of parameter uncertainties.
Results. The CO 6–5 line is detected in 13 out of 33 sources, the [C I] 1–0 in 6 out of 12, and the [C I] 2–1 in 1 out of 33. With separate deep integrations, the first unambiguous detections of the [C I] 1–0 line in disks are obtained, in TW Hya and HD 100546.
Conclusions. Gas-phase carbon abundance reductions of a factor 5–10 or more can be identified robustly based on CO and [C I] detections, assuming reasonable constraints on other parameters. The atomic carbon detection towards TW Hya confirms a factor 100 reduction of $[C]/[H]_{gas}$ in that disk, while the data are consistent with an ISM-like carbon abundance for HD 100546. In addition, BP Tau, T Cha, HD 139614, HD 141569, and HD 100453 are either carbon-depleted or gas-poor disks. The low [C I] 2–1 detection rates in the survey mostly reflect insufficient sensitivity to detect T Tauri disks. The Herbig Ae/Be disks with CO and [C II] upper limits below the models are debris disk like systems. A roughly order of magnitude increase in sensitivity compared to our survey is required to obtain useful constraints on the gas-phase [C]/[H] ratio in most of the targeted systems.

Key words. protoplanetary disks; surveys; submillimeter: planetary systems

1. Introduction

Carbon is one of the most abundant elements in the Universe, and is central to interstellar and terrestrial chemistry, and to planetary climate (Henning & Salama 1998; Unterborn et al. 2014). The carbon content of planets is determined by chemical and physical processes before and during the protoplanetary disk stage. To elucidate this stage-setting for planetary compositions, we present a survey of carbon reservoirs in 37 protoplanetary disk systems, including the first firm detections of submillimetre atomic carbon lines from disks.

The carbon budget in inter- and circumstellar material broadly consists of refractory – e.g., graphite or amorphous carbon – and volatile material – atoms, simple and complex molecules and ices. There is evidence for a rapid recycling between these (Jones 2014). The elemental abundance of gas-phase carbon with respect to hydrogen, $[C]/[H]_{gas}$, in the interstellar medium is $(1-2)\times10^{-4}$ (Cardelli et al. 1996; Parvathi et al. 2012), while the solar value is 2.69×10^{-4} (Asplund et al. 2009). This implies that, in the ISM, volatile and refractory reservoirs each contain about 50% of elemental carbon. A smaller fraction of interstellar carbon atoms, up to $\lesssim 5\%$, are bound in polycyclic aromatic hydrocarbon molecules (PAHs, Tielens 2008).

In the surface layers of protoplanetary disks, with increasing shielding from (inter)stellar ultraviolet photons C^+, C^0 and CO are the dominant gas-phase carbon carriers. Depending on the ionization state, chemical history and gas temperature, CO_2 and small hydrocarbons may carry large fractions of the volatile carbon (e.g., Bergin et al. 2014; Pontoppidan & Blevins 2014). At

low dust temperatures (below ~ 25 K for CO), the molecular carriers form icy layers on dust, where they can be further processed into complex organics which may evaporate when brought into warmer conditions. Vertical and radial mixing may give rise to a flow of carbon from the warm, tenuous gas in the disk atmosphere into cold, icy reservoirs which evolve and migrate into the inner disk, where volatile and perhaps even refractory carbon is channeled into the gas phase (e.g., Lee et al. 2010; Pontoppidan et al. 2014). The co-evolution of the various reservoirs is reflected in the gas-phase elemental abundance of carbon in the outer disk atmosphere, where volatiles likely cannot return to once locked in large icy grains and transported to the inner disk.

Observational estimates of the carbon budget in disks are difficult. The gas phase is the most accessible, with CO being the dominant reservoir in molecular gas. However, the disk-averaged CO abundance can be much less than the canonical value of $CO/H_2 \approx 10^{-4}$ due to the abovementioned freezeout and due to photodissociation in the upper layers (e.g., van Zadelhoff et al. 2001; Dutrey et al. 2003; Chapillon et al. 2010). This, combined with optical depth effects, makes recovering the elemental $[C]/[H]_{gas}$ from CO alone tricky.

Neutral and ionized atomic carbon, C^0 and C^+ (noted [C I] and [C II] where line emission is concerned), consecutively become the main gaseous carbon reservoirs in the UV-irradiated surface layers of the disk. However, [C II] cannot be observed from the ground and *Herschel* Space Observatory data contain emission from residual envelope material around disks (Fedele et al. 2013b,a; Dent et al. 2013). Neutral atomic carbon may also have a non-disk emission component, but this is easier to check as the observations are resolved in velocity and additional pointings can be taken. It is thus a promising tracer of the carbon abundance in disk atmospheres, but its disk contribution has not yet been unambiguously detected (Chapillon et al. 2010; Panić et al. 2010; Casassus et al. 2013; van der Wiel et al. 2014; Tsukagoshi et al. 2015).

Through comprehensive modelling, the total gas-phase abundance of carbon was found to be depleted by a factor of 2 to 10 with respect to an adopted volatile carbon abundance of $[C]/[H]_{gas} = 2.4 \times 10^{-4}$ in the HD 100546 disk (Bruderer et al. 2012). For the T Tauri disk system TW Hya, Favre et al. (2013) inferred a deficiency of up to two orders of magnitude in carbon abundance, based on $C^{18}O$ observations and a thus far unique bulk gas mass measurement via HD (Bergin et al. 2013). However, the $C^{18}O$-to-H_2 conversion may be impacted somewhat by isotopolog-selective CO photodissociation (Miotello et al. 2014).

We observed [C I] towards a large number of disks using the *Atacama Pathfinder EXperiment* (APEX) telescope at Cerro Chajnantor. We also present deep follow-up observations which resulted in disk detections. In our analysis, we focus on the disk atmosphere, where physical-chemical models allow to relate observations of [C I] and CO emission to the total gas-phase elemental carbon abundance.

2. Observations

2.1. Sample selection

The disks targeted in our survey (Table 1) are some of the closest and best studied ones. The main selection criteria were observability with APEX, the availability of supplementary data, and proximity to the Solar System. The spectral types range from late-B (HD 141569) to mid-M (Haro 6-5B, Sz 33).

Studies of disks with single dish instruments are complicated because the large beam can capture extended emission from a surrounding cloud. The current sample includes a number of sources for which previous single dish observations of CO and other species have demonstrated that most of the emission originates from the disk (e.g., Thi et al. 2004; van Kempen et al. 2007; Panić & Hogerheijde 2009; Kastner et al. 2008; Zuckerman et al. 1995). The observed sample includes protoplanetary disks with no known inner hole (e.g., HD 163296) as well as transitional disks with inner holes of up to several tens of au in radius (e.g., HD 100546, HD 169142). Since the disk emission component is dominated by the outer disk, which has similar characteristics in both types of sources, the presence or absence of such holes is of little importance for the purposes of this study. After the initial shallow survey, HD 97048, HD 100546 and TW Hya were chosen for deep follow-up integrations.

2.2. APEX observations

The shallow survey observations of 37 disks were carried out with the 2×7-pixel CHAMP$^+$ (Kasemann et al. 2006) and the single-pixel FLASH (Heyminck et al. 2006) instruments on APEX (Güsten et al. 2006) during several runs from 2008 until 2013. The CHAMP$^+$ observations targeted the [C I] 2–1 line at 809 GHz with the high-frequency array, with the ^{12}CO 6 – 5 line observed simultaneously in the low frequency array. The FLASH observations targeted [C I] 1–0. Deep FLASH follow up integrations on the [C I] 1–0 line towards HD 100546, HD 97048 and TW Hya were carried out in 2014. The backends used were AFFTS (CHAMP$^+$, with a highest resolution channel spacing of 0.18 MHz or 0.11 km s^{-1} at 492 GHz) and XFFTS (FLASH, 0.04 MHz or 0.02 km s^{-1}). The targeted [C I] and CO lines are summarized in Table 3. Diffraction-limited beam sizes range from 8″ to 13″. Most CHAMP$^+$ observations were taken in single pointing mode, with a typical wobbler switch of 2′ in azimuth. CHAMP$^+$ has a central pixel, with the other six radially offset by 18″ (14″) at 660 GHz (850 GHz) in a hexagonal pattern. Raster mapping was used for AA Tau, BP Tau, DL Tau, GG Tau, RY Tau, HD 36112 and Haro 65 B. The additional sky coverage was used to check for extended emission.

Typical survey observations had 10 to 400 scans with individual exposure times of 0.1 to 0.5 minutes and on-source exposure times of 10 to 60 minutes. The column of precipitable water vapour was typically 0.3 mm H_2O, but as low as 0.1 and as high as 0.7 during some observations. Smoothed to $dv = 0.17$ km s^{-1}, the median RMS noise was 0.31 K for CO 6–5, 0.18 K for [C I] 1–0 and 0.67 K for [C I] 2–1. Initial processing was done using the APECS software (Muders et al. 2006). Baseline subtraction and other higher level reductions were done with GILDAS/CLASS[1]. Telescope parameters were obtained from Güsten et al. (2006). The intensities, $T_A^\star$, are corrected for atmospheric and radiative loss and spillover; they can be converted to main beam temperature via $T_{mb} = (F_{eff}/\eta_{mb}) \times T_A^\star$, where $F_{eff} = 0.95$. Based on Güsten et al. (2006), the Kelvin-to-Jansky conversion and main beam efficiency at 650 GHz are 57 Jy K^{-1} and 0.53, respectively. At 812 GHz, they are 70 Jy K^{-1} and 0.43. At 491 GHz, the conversion factor is 49 Jy K^{-1} and $\eta_{mb} = 0.59$.

All sources and flux values from our survey are listed in Table 1 and shown in Fig. 1, including the detections of [C I] 1–0 towards TW Hya and HD 100546. The spectra are presented in Fig. 2, and an example of extended emission in Fig. 3.

[1] http://www.iram.fr/IRAMFR/GILDAS

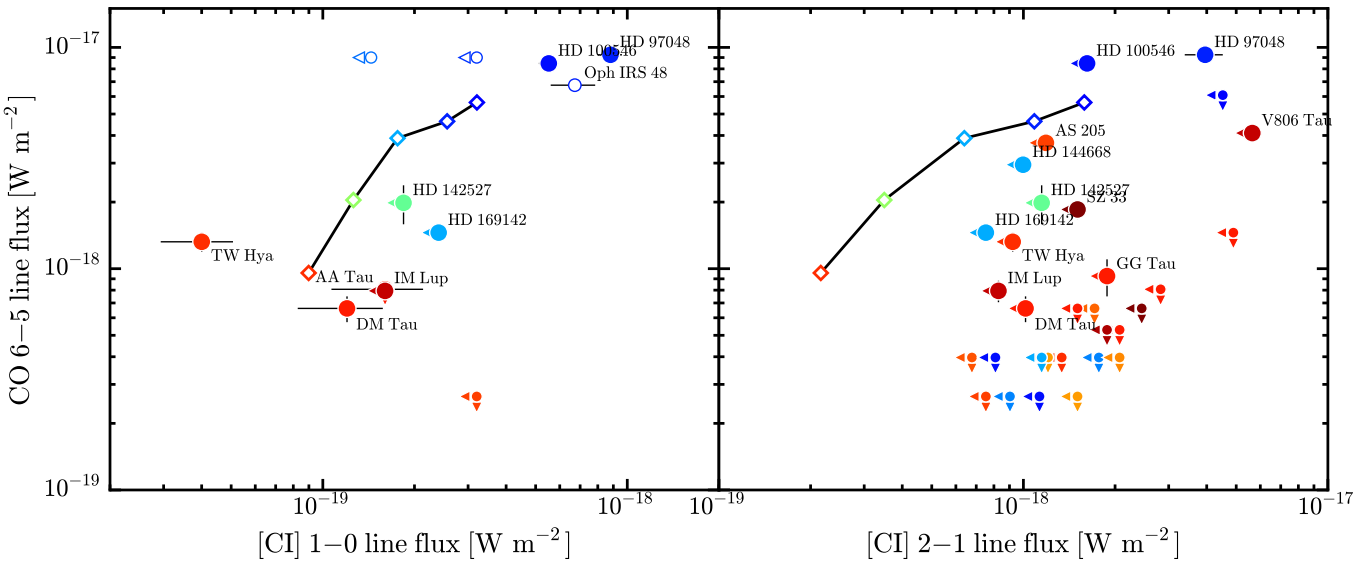

Fig. 1. Fluxes and upper limits (at 3σ confidence) from our APEX observations of the [C I] 1–0 and 2–1 and the CO 6–5 transitions. Large circles indicate sources with a detection on at least one axis. Empty symbols mark sources for which only the [C I] 1–0 line was observed. CO 6–5 and [C I] 2–1 were always observed in parallel. Colours show the stellar effective temperature, with late-type stars red and early-type stars blue. The black line connects fiducial disk models from Section 4 for the stellar spectral type range of our observations (diamonds from red to blue, $T_{\rm eff} \in [4000, 12000]$ K in steps of 2000 K, assumed distance 140 pc).

2.3. Complementary data

To complement our [C I] 1–0 data for HD 142527, the CO 6–5 and [C I] 2–1 lines from Casassus et al. (2013) are included in Table 1. We also use observations of the [C II] $J = 3/2$–$1/2$ transition at 158 μm towards a number of disks, obtained with the *Herschel*/PACS low-resolution spectrometer by the GASPS (Thi et al. 2010; Meeus et al. 2012; Dent et al. 2013; Howard et al. 2013) and DIGIT (Fedele et al. 2013b) key programmes.

3. Observational results

The APEX spectra of 37 disks are shown in Fig. 2 and the measurements are summarized in Table 1. Not all lines were observed towards all disks. Emission in the CO 6–5 line was detected (observed) towards 13 (33) sources; the corresponding numbers are 6 (12) for the [C I] 1–0 line and 1 (33) for the [C I] 2–1 line. When considering detections and upper limits, sources of all spectral types cover a similar range in line flux, although the CO and [C I] detections towards Herbig disks are typically a factor of a few stronger than towards T Tauri disks.

The CO 6–5 lines are single-peaked and narrow, except for three sources which show wide, double-peaked lines. The first is HD 100546, where the line displays the same blue-over-red peak asymmetry seen in lower-J CO observations (e.g., Panić et al. 2010, where the CO 6–5 line was also previously shown). The second is HD 97048, which has a filled-in line center suggestive of a non-disk emission component. The third is IM Lup, a very large T Tauri disk (van Kempen et al. 2007; Panić et al. 2009). The CO 6–5 line has been observed previously towards a number of disks. The upper limit obtained by van Zadelhoff et al. (2001) towards TW Hya lies 30% above the detection reported in Table 1. A comparison of the six overlapping sources with Thi et al. (2001) shows good consistency, with APEX yielding improved upper limits and detections. In the case of GM Aur, our upper limit lies a factor of 1.5 below the detection from 2001, but is within its errorbars. The CO 6–5 flux detected towards HD 142527 by Casassus et al. (2013), 1.5 ± 0.9 K km s^{-1}, is roughly in the middle of the range of values across our entire sample. The values reported for HD 100546 and HD 97048 in the much larger *Herschel*/SPIRE beam by van der Wiel et al. (2014) are also consistent with our detections.

In most sources where [C I] emission is detected, the emission is extended or contaminated by the reference position. The exceptions are HD 100546 and TW Hya. These two are the first two unambiguous detections of [C I] in protoplanetary disks, with a $T_{\rm A}^{\star}$ line flux of 0.49 K km s^{-1} (S/N=10) towards HD 100546 and 0.05 K km s^{-1} (S/N=3) towards TW Hya. Gaussian fit parameters for both detections are given in Table 2. We also detect a strongly asymmetric double-peaked line towards HD 97048. This detection likely has a disk contribution, but it is difficult to quantify because of contamination issues affecting the line center. The [C I] 1–0 line is detected towards Oph IRS 48 (also known as WLY 2-48), but the line profile is asymmetric, with emission redshifted from the rest velocity of 4.6 km s^{-1} and absorption on the red side. The disk contribution can thus not be determined at the moment.

Table 2. Gaussian fit parameters for the definitive [C I] 1–0 detections.

Source	Flux (K km s^{-1})	Peak (K)	$v_{\rm lsr}$ (km s^{-1})	Width (km s^{-1})
HD 100546	0.69 ± 0.15	0.15 ± 0.12	5.6 ± 0.6	4.4 ± 0.9
TW Hya	0.05 ± 0.03	0.11 ± 0.10	2.7 ± 0.3	0.41 ± 0.36

Notes: All uncertainties are $3\,\sigma$.

The [C I] transitions have recently been surveyed with *Herschel*/SPIRE by van der Wiel et al. (2014), who report no firm detections. Generally, the [C I] 1–0 limits from APEX have better sensitivity than SPIRE, while SPIRE provides deeper lim-

Table 1. Summary of the disks and line fluxes observed with APEX.

Source	Spectral type*	d (pc)	$i_{\rm disk}$ (°)	CO 6–5 Flux $\pm 3\sigma$ (K km s^{-1})	CO 6–5 RMS (K)	[C I] 1–0 Flux $\pm 3\sigma$ (K km s^{-1})	[C I] 1–0 RMS (K)	[C I] 2–1 Flux $\pm 3\sigma$ (K km s^{-1})	[C I] 2–1 RMS (K)
AA Tau	K7[s1]	140	71[i1]	≤ 0.61	0.58	0.2 ± 0.2(e?)	0.18	≤ 1.5	1.4
AS 205	K5+K7+M0[s12]	125[d1]	$15 + 20$[i2]	2.8 ± 0.3	0.33	…	…	≤ 0.63	0.66
AS 209	K4[s2]	119 ± 6[d2]	56[i3]	≤ 0.3	0.26	…	…	≤ 0.36	0.38
BP Tau	K7[s3]	140	30[i4]	≤ 0.4	0.42	…	…	≤ 1.1	1.1
CS Cha	K6[s4]	150[d3]	60[i5]	≤ 0.3	0.34	…	…	≤ 0.71	0.73
CV Cha	K0[s5]	150[d3]	35[i6]	≤ 0.3	0.33	…	…	≤ 0.64	0.66
DL Tau	K7	140	38[i7]	≤ 0.4	0.36	…	…	≤ 1.0	1.0
DM Tau	M1[s6]	140	32[i4]	0.5 ± 0.2	0.22	0.15 ± 0.14(e?)	0.09	≤ 0.54	0.51
GG Tau A	M0+M2+M3[s11]	140	37[i8]	0.7 ± 0.4	0.41	…	…	≤ 1.0	1.0
GM Aur	K3[s6]	140	56[i4]	≤ 0.5	0.52	…	…	≤ 0.91	0.94
HD 100453	A9	122 ± 10[d4]	…	≤ 0.2	0.22	…	…	≤ 0.4	0.38
HD 100546	B9	97 ± 4[d4]	44[i9]	6.4 ± 0.3	0.18	0.69 ± 0.15	0.12	≤ 0.86	0.54
HD 104237	A4	116 ± 5[d4]	18[i10]	…	…	≤ 0.18	0.02	…	…
HD 139614	A8	140 ± 5[d6]	20[i11]	≤ 0.3	0.29	…	…	≤ 0.61	0.63
HD 141569	A0	116 ± 7[d4]	51[i12]	≤ 0.2	0.16	…	…	≤ 0.6	0.63
HD 142527	F6	230 ± 50[d4]	20[i13]	1.5 ± 0.9[C13]	…	≤ 0.23	0.21	≤ 0.6[C13]	…
HD 144668	A7	160 ± 15[d4]	58[i14]	2.2 ± 0.1(e)	0.08	…	…	≤ 0.53	0.55
HD 163296	A1	120 ± 10[d4]	45[i15]	…	…	≤ 0.4	0.39	…	…
HD 169142	A5	145 ± 5[d6]	8[i10]	1.1 ± 0.2	0.21	≤ 0.3	0.27	≤ 0.4	0.37
HD 36112 (MWC 758)	A8	280 ± 55[d4]	21[i16]	≤ 0.3	0.32	…	…	≤ 0.94	0.97
HD 38120	A5[s13]	480 ± 175[d4]	…	≤ 0.2	0.19	…	…	≤ 0.48	0.50
HD 50138	B9?	390 ± 70[d4]	…	≤ 0.3	0.29	…	…	≤ 0.43	0.45
HD 97048	A0e	160 ± 15[d4]	43[i17]	7.0 ± 0.3	0.30	1.4 ± 0.3	0.07	2.1 ± 0.9	0.75
Haro 6-5 B	M4	145[d7,d8]	74[i18]	≤ 0.5	0.49	…	…	≤ 1.3	1.4
IM Lup	M0	155 ± 8[d2]	54[i19]	0.6 ± 0.2	0.23	≤ 0.2	0.19	≤ 0.44	0.46
LkHα 264	K5.5[s7]	360 ± 30[d9]	20[i20]	≤ 0.2	0.15	≤ 0.4	0.40	≤ 0.4	0.38
RY Tau	K1[s3]	140	65[i21]	≤ 0.3	0.31	…	…	≤ 1.1	1.1
Sz 33	M3.5+M7[s8]	150[d3]	…	1.4 ± 0.4	0.43	…	…	≤ 0.8	0.67
Sz 41	K7+M2.5[s8]	150[d3]	…	≤ 0.5	0.43	…	…	≤ 0.8	0.86
T Cha	K0[s2]	108 ± 9[d10]	67[i22]	≤ 0.2	0.23	…	…	≤ 0.8	0.78
TW Hya	K7[s9]	56 ± 7[d11]	7[i23]	1.0 ± 0.3	0.28	0.05 ± 0.03	0.10	≤ 0.49	0.51
V806 Tau	M0	140	…	3.1 ± 0.8	0.83	…	…	≤ 3.0	3.1
V892 Tau	A0	140	60[i24]	4.6 ± 0.8(e)	0.77	…	…	≤ 2.4	2.5
VZ Cha	K7[s5]	150[d3]	…	≤ 1.1	1.0	…	…	≤ 2.6	2.3
Oph IRS 48 (WLY 2-48)	A0[s10]	139 ± 6[d12]	50[i25]	…	…	0.8 ± 0.4(e?)	0.18	…	…
Median		140	45		0.31		0.21		0.66

Notes: All uncertainties and upper limits are at 3σ confidence. Extended emission is indicated with '(e?)'. The intensity scale is $T_{\rm A}^\star$ (K). Flux upper limits were calculated as RMS$\times\sqrt{N_{\rm chan}\times\delta v}$ over a linewidth of δv = 5 km s^{-1}, and 3σ RMS values are given for a dv = 0.17 km s^{-1} channel spacing. Spectral types without references are from SIMBAD. * – components of arcsecond-scale multiples are separated with a plus sign; [C13] – Casassus et al. (2013); [T15] – Tsukagoshi et al. (2015); [d1] – Pontoppidan et al. (2011); [d2] – Lombardi et al. (2008); [d3] – Knude & Hog (1998); [d4] – van Leeuwen (2007); [d5] – van Boekel et al. (2005); [d6] – Acke & van den Ancker (2004); [d7] – Torres et al. (2009); [d8] – Torres et al. (2012); [d9] – Andersson et al. (2002); [d10] – Torres et al. (2008); [d11] – Wichmann et al. (1998); [d12] – Mamajek (2008); [i1] – Cox et al. (2013); [i2] – Salyk et al. (2014); [i3] – Koerner & Sargent (1995); [i4] – Simon et al. (2000); [i5] – Espaillat et al. (2007); [i6] – Hussain et al. (2009); [i7] – Guilloteau et al. (2011); [i8] – Guilloteau et al. (1999); [i9] – Walsh et al. (2014a); [i10] – Malfait et al. (1998); [i11] – Matter et al. (2014); [i12] – Weinberger et al. (1999); [i13] – Canovas et al. (2013); [i14] – Preibisch et al. (2006); [i15] – de Gregorio-Monsalvo et al. (2013); [i16] – Isella et al. (2010); [i17] – Doucet et al. (2007); [i18] – Stark et al. (2006); [i19] – Panić et al. (2009); [i20] – Carmona et al. (2007); [i21] – McCleary et al. (2007); [i22] – Huelamo et al. (2015); [i23] – Qi et al. (2004); [i24] – Monnier et al. (2008); [i25] – van der Marel et al. (2013); [s1] – White & Ghez (2001); [s2] – Torres et al. (2006); [s3] – Bertout et al. (2007); [s4] – Luhman (2004); [s5] – Torres et al. (2006); [s6] – Bertout et al. (2007); [s7] – Luhman (2001); [s8] – Daemgen et al. (2013); [s9] – Rucinski & Krautter (1983); [s10] – Brown et al. (2012); [s11] – Di Folco et al. (2014); [s12] – Eisner et al. (2005); [s13] – Meeus et al. (2012)

its to the 2–1 line. However, SPIRE could not spectrally or spatially resolve disk emission. Its beam at 809 GHz was 26″, compared to 8″ for APEX. The tentative SPIRE detection of [C I] 2–1 for HD 100546 lies within errorbars of our upper limit, which is a re-evaluation of the data reported by Panić et al. (2010). For HD 100453, HD 169142, HD 36112 and HD 50138, the 2–1 limits are similar. We also detect [C I] 2–1 towards HD 97048, but above the upper limit of van der Wiel et al. (2014), suggesting that the emission is extended and was subtracted out in the SPIRE analysis where off-source spaxels were used as a reference pointing. This also makes our [C I] 1–0 detection towards that source suspect. For RY Tau, the SPIRE limit is a factor of five deeper than the APEX one. The proximity of TW Hya allowed our deep APEX integrations to yield a detection of the faint [C I] 1–0 transition and the lowest distance-corrected upper limit on the 2–1 line in our survey.

DM Tau shows purely on-source CO 6–5 emission and extended [C I] emission, as shown in Fig. 3. For CO, a broad line consistent with the disk inclination is detected on-source while the off-source position is clean. The on-source [C I] emission has two narrow components, one strong and narrow peak due to extended emission at (9.3 ± 0.1) km s^{-1}, also seen in the reference spectrum, and the other at (6.3 ± 0.2) km s^{-1} probably originating in a compact envelope. The latter matches the CO detection, but is narrower. Our on-source detection of [C I] 1–0 is within the errorbars of the value from Tsukagoshi et al. (2015), however the [C I] line from this inclined disk is single-peaked and narrower than the CO line, suggesting an envelope or wind contribution. The same narrow kinematic components are seen for

this source in the low-J CO lines (Guilloteau & Dutrey 1994). Aside from having the 9 km s^{-1} component, the low-J CO isotopolog lines at 6 km s^{-1} are double-peaked and the ^{12}CO 2–1 line shows an additional narrow emission peak at the systemic velocity. The CO 6–5 line appears to originate purely in the disk. Follow-up observations are needed to firmly establish the origin of the [C I] 1–0 emission towards DM Tau.

A single-peaked [C I] 1–0 line is also marginally detected towards AA Tau. No offset position was observed, but given that this disk is seen edge-on and accordingly has very broad emission lines (e.g. Brown et al. 2013), the narrow line is likely cloud emission.

The CO 6–5 line towards HD 144668 is uniform across all seven CHAMP$^+$ pixels, with a flux increase towards northern positions, suggesting the line originates entirely in an extended cloud. The T Tauri systems AS 205, Sz 33 and V806 Tau have very strong CO 6–5 emission, but display no emission in the off-source CHAMP$^+$ pixels, ruling out extended emission. Their single-peaked on-source line profiles suggest a contribution from a remnant envelope or a disk wind (Pontoppidan et al. 2011; Salyk et al. 2014). AS 205 is a hierarchical T Tauri triple within 1.3″ (Eisner et al. 2005). For AS 205A, single-peaked profiles are also seen in ro-vibrational CO lines (Bast et al. 2011; Brown et al. 2013).

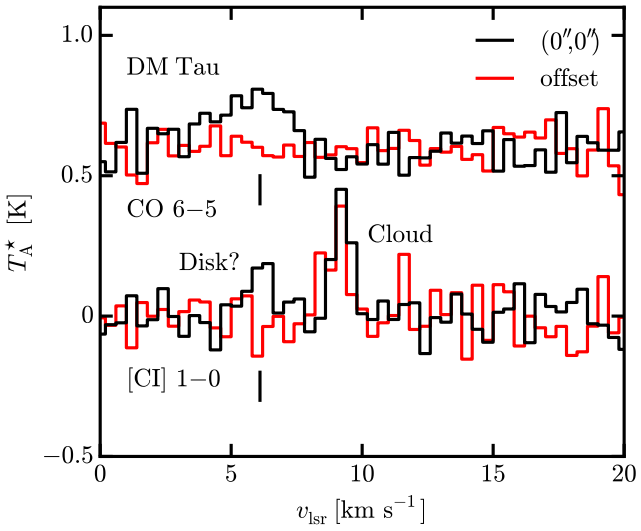

Fig. 3. The [C I] 1–0 and CO 6–5 lines observed towards DM Tau (black) and typical offset positions (red; +30″, 0″ for [C I], +18″, +6″ for CO). The [C I] line towards the source is single-peaked and narrower than CO 6–5. The spectra are binned to 0.4 km s^{-1} per channel.

4. Modelling

Our next goals are to relate the observed [C I] and CO emission to the elemental [C]/[H]$_{gas}$ ratio in the warm atmosphere of a disk, where surface chemistry is unimportant, and to understand the low detection rates and upper limits in our survey. To this end, we make use of the DALI physical-chemical code (Bruderer et al. 2012; Bruderer 2013). Starting with a parameterized gas and dust density distribution (Section 4.1), and an input stellar spectrum (Section 4.2), DALI first solves the continuum radiative transfer to determine the UV radiation field and the dust temperature. This yields an initial guess for the gas temperature, which is the starting point of an iterative sequence in which the chemistry and thermal balance are calculated. Once the solution is converged, the code can output emission maps, spectra and integrated fluxes. We present below a grid of generic models, with parameter ranges covering the source sample. All observables are hereafter normalized to 140 pc. Tailored models for TW Hya and HD 100546, with detailed fitting of the carbon abundance, will be presented in a companion paper (Kama et al. submitted).

4.1. Disk parameters

The disk density structure in our version of DALI is fully parameterized. The gas-to-dust mass ratio is $\Delta_{gas/dust}$. The surface density has the standard form of a power law with an outer exponential taper:

$$\Sigma_{gas} = \Sigma_c \cdot \left(\frac{r}{R_c}\right)^{-\gamma} \cdot \exp\left[-\left(\frac{r}{R_c}\right)^{2-\gamma}\right]. \quad (1)$$

To simulate an inner cavity, material can be removed inside of some radius r_{hole}. The scaleheight angle, h, at distance r is given by $h(r) = h_c\,(r/R_c)^{\psi}$, such that the scaleheight is $H = h \cdot r$, and the vertical density structure of the small grains is

$$\rho_{d,small} = \frac{(1-f)\,\Sigma_{dust}}{\sqrt{2\pi}\,r\,h} \times \exp\left[-\frac{1}{2}\left(\frac{\pi/2-\theta}{h}\right)^2\right], \quad (2)$$

where f is the mass fraction of large grains and θ is the opening angle from the midplane as viewed from the central star. The settling of large grains is prescribed as a fraction $\chi \in (0, 1]$ of the scaleheight of the small grains, so the mass density of large grains is similar to Eq. 2, with f replacing $(1 - f)$ and χh replacing h. The vertical distribution of gas is calculated in each grid cell as $\rho_{gas} = \Delta_{g/d} \times \rho_{d,small} \times [1 + f/(1 - f)]$. The latter factor adds the mass of large grains as if they were not settled, to preserve the global $\Delta_{gas/dust}$. The ranges and fiducial values of all parameters in our model grid are given in Table 4. The range of R_c, ψ and γ are guided by results from homogeneous sample fitting studies (Andrews et al. 2009, 2010). The main fiducial disk model has a total mass of $10^{-2}\,M_\odot$ and a reference surface density of $\Sigma_c = 5.5\,g\,cm^{-2}$ at $R_c = 50$ au. We also calculate some models for a very small fiducial disk, with $R_c = 10$ au and $\Sigma_c = 140\,g\,cm^{-2}$.

4.2. Stellar parameters and accretion rates

The stellar spectra were approximated as pure blackbodies. For consistency, the T_{eff} of a star was uniquely related to a combination of mass, radius and luminosity using the PISA pre-main-sequence evolutionary tracks of Tognelli et al. (2011) at a model age of 5 Myr. We adopt a $T_{eff} = 10000$ K star as representative for the Herbig Ae/Be group (spectral types B, A, F) and a 4000 K star with UV-excess for the T Tauri group (G, K, M). For $T_{eff} = 4000$ K, accretion at a rate of $\dot{M} = 10^{-8}\,M_\odot\,yr^{-1}$ was assumed to release energy in blackbody emission at the stellar photosphere at $T_{acc} = 10000$ K. The relevant stellar and ultraviolet luminosities are listed in Table 5. Lyman α radiation was not explicitly considered. This does not affect the photodissociation of CO or the -ionization of C^0, as only photons at $\lesssim 1100$ Å are important. The fiducial X-ray luminosity adopted in the models, $L_X = 10^{29}$ erg s^{-1}, is close to the median value for the classical T Tauri star sample from Neuhäuser et al. (1995).

Table 3. The atomic and molecular lines used in this paper.

Species	Transition	E_u (K)	A_{ul} ($^{-1}$)	n_{crit} (H_2 at 100 K) (cm^{-3})	ν (GHz)	θ_{beam} ($''$)	Instrument
C^0	[C I] $^3P_1$–$^3P_0$	23.6	7.880×10^{-8}	5×10^2	492.16065	13	APEX/FLASH
C^0	[C I] $^3P_2$–$^3P_1$	62.5	2.650×10^{-7}	5×10^2	809.34197	8	APEX/CHAMP$^+$
CO	CO 6–5	116.2	2.137×10^{-5}	3×10^5	691.47308	10	APEX/CHAMP$^+$
C^+	[C II] $^2P_{3/2}$–$^2P_{1/2}$	91.21	2.300×10^{-6}	5×10^3	1900.5369	11	*Herschel*/PACS

Table 4. The fiducial values and grid ranges of the model parameters.

Parameter	Fiducial	Range	Units
γ	1.0	[0.8, 1.5]	
R_c	50, 10	[10, 130]	(au)
Σ_c	5.5	[0.055, 55]	(g cm^{-2})
$\Sigma_c(R_c$=10 au)	140	single value	(g cm^{-2})
M_{disk}	10^{-2}	[10^{-4}, 10^{-1}]	($M_\odot$)
$\Delta_{gas/dust}$	100	[10, 1000]	
h_c	10	[0.05, 0.20]	
ψ	0.2	[0.05, 0.3]	
χ	0.5	[0.1, 1.0]	
f	0.90	[0.20, 0.99]	
r_{hole}	0	[0, 75]	(au)
L_X, T_X	7.94×10^{28}	single value	(erg s^{-1})
L_X, T_X	7×10^7	single value	(K)
ζ_{cr}	5	[0.05, 500]	(10^{-17} s^{-1})
[C]/[H]$_{gas}$(R_c=50, 10 au)	1.35	[0.01, 2]	($\times 10^{-4}$)
i	60	[0, 90]	($^\circ$)

Notes: Unless explicitly noted, all variations are around the R_c=50 au fiducial model. For variations of R_c, we keep the disk mass fixed at 10^{-2} $M_\odot$ and accordingly adjust $\Sigma_c(R_c)$.

4.3. The chemical network

The adopted chemical network is based on UMIST 06 (Woodall et al. 2007). It consists of 109 species, including neutral and charged PAHs, and 1463 individual reactions. In addition to two-body reactions, the code includes freezeout, thermal and photodesorption, and photodissociation and -ionization. Hydrogenation is the only grain surface reaction considered. This has no impact on the chemistry of the disk atmosphere species considered in this work.

We adopt a fiducial gas-phase elemental carbon and oxygen abundance of [C]/[H]$_{gas}$ = 1.35×10^{-4} and [O]/[H]$_{gas}$ = 2.88×10^{-4}, respectively. These values are close to the medians observed in diffuse and translucent interstellar clouds by UV absorption lines of C^+ and O^0. The total elemental abundance of carbon is still subject to considerable uncertainties. The solar abundance is 2.69×10^{-4} (Asplund et al. 2009), whereas that of the material from which the Solar System formed is estimated at 2.88×10^{-4} (Lodders 2003). Values as high as 4×10^{-4} have been advocated for the cosmic carbon abundance in the solar neighborhood (Parvathi et al. 2012). [C]/[H]$_{gas}$ sets the amount of carbon that is cycled in our model between the volatile phases, i.e., atoms, molecules and ices. The refractory carbonaceous dust reservoir is not explicitly considered. PAHs, which absorb stellar UV photons, are a major gas heating agent in the disk atmosphere (e.g., Bakes & Tielens 1994; Habart et al. 2004). Following typical values inferred from observations (0.1 . . . 0.01 Geers et al. 2006; Kamp 2011, and references therein), the PAH abundance was set to 0.1 of the interstellar value of [PAH]/[H] ~ 10^{-7}. When varying [C]/[H]$_{gas}$, we also vary [O]/[H]$_{gas}$ to keep the C/O ratio constant. Keeping [O]/[H]$_{gas}$ fixed would make the C^0 abundance more strongly dependent on [C]/[H]$_{gas}$, as more oxygen would be available to bind up carbon.

Table 5. The total and ultraviolet stellar luminosities.

Spectrum	CO ph.dissoc. 91.2 . . . 110 nm ($L_\odot$)	Broadband UV 91.2 . . . 200 nm ($L_\odot$)	Stellar L_{tot} ($L_\odot$)
4000 K	1.3×10^{-11}	5.8×10^{-6}	0.38
4000 K+UV	1.4×10^{-4}	1.2×10^{-2}	0.55
6000 K	5.7×10^{-6}	2.0×10^{-2}	9.88
6000 K+UV	1.6×10^{-4}	3.4×10^{-2}	10.1
8000 K	1.7×10^{-3}	5.7×10^{-1}	29.4
10000 K	2.6×10^{-2}	2.2×10^{0}	34.0
12000 K	2.3×10^{-1}	8.2×10^{0}	59.6
TW Hya[r1]	6.7×10^{-5}	7.5×10^{-3}	≈0.3
HD 100546[r2]	1.5×10^{-2}	9.1×10^{0}	≈30

Notes: Temperatures refer to the model stars described in Section 4.2, based on the pre-main sequence tracks of Tognelli et al. (2011). The excess UV for the 4000 and 6000 K stars is for an accretion rate $\dot{M} = 10^{-8}$ $M_\odot$ yr^{-1}, with the energy released on the stellar surface at 10000 K effective temperature. The Lyman α luminosity of TW Hya, integrated from 121 to 122 nm, is 5.1×10^{-3} $L_\odot$. *References:* [r1] – France et al. (2014), [r2] – Bruderer et al. (2012).

5. Modelling results

In Appendix A, Figs. A.1 and A.2, we present the gas density, gas and dust temperature, and the extinction for the fiducial disk models. The fiducial Herbig disk is substantially warmer, notably the CO freezeout zone ($T_{dust} \lesssim 25$ K) is much larger in the T Tauri disk than in the Herbig Ae/Be one.

5.1. Origin of the CO, [C I] and [C II] emission

Abundance and emission contribution maps for the CO 6–5, [C I] 1–0, [C I] 2–1 and [C II] 158 μm transitions are shown in Fig. 4. The exterior layers of a protoplanetary disk form a complex photodissociation region (PDR), but covering a much larger range of n_{gas}, G_0 and dust properties than standard PDRs in the interstellar medium (Tielens & Hollenbach 1985; van Dishoeck et al. 2006). The general outcome is outside-in layering where the dominant gas-phase carbon reservoir switches from C^+ to C^0 and then CO. The rotational lines of CO are optically thick to high J levels and thus probe the surface area and temperature of the disk, while the optically thin [C I] and [C II] lines are "carbon counters" for the disk atmosphere.

The emission of the CO 6–5 transition (E_u = 116.2 K) originates primarily in the outer disk, but has contributions from the entire warm molecular layer. It is optically thick out to several hundred astronomical units. The [C I] 1–0 and [C I] 2–1 transitions have lower upper level energies compared to CO 6–5 by a

factor of a few, while the C^0 atom has its peak abundance exterior to that of CO. Thus, the [C I] lines predominantly originate in the surface layers of the outer disk, with a small contribution from the inner disk. Carbon is ionized everywhere exterior to the C^0 layer and its optically thin emission probes the warm tenuous gas around the disk. Atomic carbon offers the clear advantage of counting carbon atoms in the warm atmosphere of the disk. The disk contribution can be verified with additional pointings and the line profile shape. [C II] is more susceptible to nebular contamination and is usually spatially and spectrally unresolved, while CO usually suffers from optical depth issues.

5.2. The degeneracy of [C]/[H]$_{\rm gas}$ with other parameters

In Fig. 5, the effect of various disk model parameters on the emergent line fluxes of CO, [C I] and [C II] is shown, and compared with the effect of varying [C]/[H]$_{\rm gas}$ for the stars representing the T Tauri and Herbig Ae/Be classes. The parameters with the smallest influence on the line fluxes include the flaring parameters (ψ and $h_{\rm c}$), the mass and scaleheight ratio of large to small grains (f and χ), the inner hole size ($r_{\rm hole}$) and the cosmic ray ionization rate ($\zeta_{\rm cr}$). Considering the [C I] 1–0 line flux, all these parameters individually lead to variations of a factor of no more than two within the full range of values listed in Table 4. These parameter dependencies are discussed in more detail in Appendix B.

The disk surface density scaling ($\Sigma_{\rm c}(R_{\rm c})$ for $R_{\rm c}$ = const) and power law index (γ) both yield up to a factor of five variations of line flux, but the corresponding change in $\Sigma_{\rm c}(R_{\rm c})$ is equivalent to two orders of magnitude in disk mass.

As the mass of dust contributing to the optical through millimeter opacity is known to reasonable accuracy, the next main uncertainty is the gas to dust ratio ($\Delta_{\rm gas/dust}$). A change of one order of magnitude in this ratio induces a change of a factor of three in the [C I] lines, and a factor of two in the CO and [C II]. This is a comparable influence to one order of magnitude in [C]/[H]$_{\rm gas}$. A gas-phase carbon underabundance of one to two orders of magnitude, such as has been proposed for TW Hya (Favre et al. 2013), is easily distinguishable from all the reasonable parameter variations explored above. Furthermore, while factor of two changes in [C]/[H]$_{\rm gas}$ are easily masked by various parameter uncertainties, a carbon underabundance of one order of magnitude can be readily identified as long as $R_{\rm c}$ is determined to within a factor of two and the disk flaring type – flat, with $\psi \approx 0.1$; or flared, with $\psi \gtrsim 0.2$ – is known. Both of these are reasonable requirements, especially as the spatial resolution of ALMA will allow to determine the radial size of disks within a few hundred parsecs to much better than a factor of two.

In summary, if the large-scale radial structure of the disk is known to a level reasonably expected in the ALMA era, and the flaring state of the disk is known (from the mid- to far-infrared SED, for example), a gas-phase carbon underabundance of an order of magnitude or more can be distinguished from reasonable variations of individual parameters. A more accurate estimate of [C]/[H]$_{\rm gas}$ will require detailled modelling of the disk of interest, to avoid unfavourable combinations of parameter uncertainties. Masking an underabundance as severe as two orders of magnitude in [C]/[H]$_{\rm gas}$ would require unreasonable fine-tuning of such parameter variations, however.

5.3. Comparison with observations

In Fig. 6, we compare the APEX observations of CO 6–5, [C I] 1–0, and [C I] 2–1with a grid of DALI models. We also show the literature [C II] fluxes. To cover the spectral types in our sample, we vary the stellar properties from a $T_{\rm eff}$ 4000 K T Tauri star with UV excess to a 12000 K Herbig star, in steps of 2000 K. The luminosities are given in Table 5. For the $T_{\rm eff}$ = 4000 K and 10000 K stars, we show two disk sizes, $R_{\rm c}$ = 10 and 50 au, and vary the gas-phase carbon abundance, [C]/[H]$_{\rm gas}$ $\in [10^{-6}, 2\times10^{-4}]$. The total disk mass is fixed at $M_{\rm disk} = 10^{-2}\,M_{\odot}$, except when varying the gas-to-dust ratio by a factor of ten, where we keep the dust mass fixed. All fluxes are normalized to a distance of 140 pc, and colour-coded for the stellar effective temperature.

As detailed in the following two subsections, most of our observations fall within reasonable variations of the model parameters. Due to limited sensitivity, none of the observed lines strongly constrains the carbon abundance in most sources. A subset of sources are brighter than the models at some of the targeted frequencies. These are very flared disks with large inner cavities (HD 142527, HD 97048, Oph IRS 48) or with a powerful jet ([C II] towards DG Tau).

5.3.1. T Tauri systems (spectral types G, K, M)

CO 6–5: The observations almost entirely fall between the fiducial $R_{\rm c}$ = 10 and 50 au models with an ISM-like [C]/[H]$_{\rm gas}$. This underlines the importance of knowing the radial extent of the gas disk for constraining [C]/[H]$_{\rm gas}$. The three disks with the deepest CO limits (BP Tau, T Cha) or detections (TW Hya) may be carbon-depleted, while the three disks with the brightest detections (AS 205, Sz 33, V806 Tau) are likely contaminated by envelope or disk wind emission.

[C I] 1–0: The detection towards TW Hya confirms its low [C]/[H]$_{\rm gas}$ ratio, while the other four observations lie above most of the models. The two detections among these four are likely residual envelope or molecular cloud emission, as the line profiles are very narrow. Narrow lines are unexpected for both AA Tau, which is a well-known edge-on disk, as well as for DM Tau, which has i=32°, and where the CO 6–5 line is substantially broader than the [C I] 1–0 (see Figure 3).

[C I] 2–1: All targeted disks with the exception of TW Hya have upper limits above the model grid. The upper limit for TW Hya does not strongly constrain [C]/[H]$_{\rm gas}$, but is consistent with the low value inferred from CO 6–5 and [C I] 1–0.

[C II] 158 μm: The upper limits from Howard et al. (2013) are generally not yet sensitive enough to lie in the model parameter space, with the exception of the datapoint for TW Hya from Thi et al. (2010). The second-lowest [C II] 158 μm upper limit is obtained for AA Tau. The point lies close to an ISM-like model [C]/[H]$_{\rm gas}$ and does not provide a strong constraint.

Additional comments: BP Tau and T Cha have distance-normalized CO 6–5 upper limits below the detection of TW Hya, which is an extremely weak CO, [C I] and [C II] emitter. Combined with the known gas disk radius of ≈215 au (Andrews et al. 2012), the CO and [C I] line fluxes for TW Hya are consistent with a factor of 10–100 underabundance of gas-phase carbon (Favre et al. 2013, Kama et al. submitted). The gas disk of BP Tau extends to ≈100 au, and the CO-based disk mass is only $M_{\rm disk} = 1.2\times10^{-3}$ (Dutrey et al. 2003). The gas disk of T Cha extends to ≈200 au (Huelamo et al. 2015). Given their considerable radial sizes, comparable to that of TW Hya, the disks of both BP Tau and T Cha thus have either a low $\Delta_{\rm gas/dust}$ or a low

$[C]/[H]_{gas}$ ratio. DM Tau and IM Lup are large disks with CO 6–5 fluxes comparable to our models with interstellar $[C]/[H]_{gas}$. GG Tau A appears similar but is a special case, as it is a large circum-triple ring – not directly comparable to any of our models (Guilloteau et al. 1999; Di Folco et al. 2014). AS 205, Sz 33 and V806 Tau have substantially larger CO 6–5 fluxes than predicted by our fiducial models, placing them close to the Herbig disks. As discussed earlier, remnant envelopes and disk winds could dominate emission in these systems. If the systems are very young, the stellar luminosity for a given $T_{\rm eff}$ could also be substantially larger.

5.3.2. Herbig Ae/Be systems (spectral types B, A, F)

CO 6–5: All non-extended, non-contaminated detections of CO around early-type stars are from group I systems, in the Meeus et al. (2001) classification of Herbig Ae/Be disks as flaring/warm (group I) and flat/cold (group II). This is consistent with the flaring disks being warmer and thus stronger emitters (see also the effects of ψ and $h_{\rm C}$ in Fig. 5). All the detected disks have inner holes – HD 97048, HD 100546 and HD 169142 (hole radii 34, 13, and 23 au, respectively, Maaskant et al. 2013; Panić et al. 2014; Walsh et al. 2014b). However, the line is not detected towards HD 139614 (5.6 au Matter et al. 2014), which has a dust mass and spectral type very similar to HD 169142 ($\approx 1{\times}10^{-4}\,M_\odot$ and A8/A5 Dent et al. 2005; Panić et al. 2008; Maaskant et al. 2013). This, combined with its large outer radius of 150 au (Matter et al. 2015), suggests a low $\Delta_{\rm gas/dust}$ or $[C]/[H]_{gas}$. Two early-type disks lie below even the late-type locus on the CO 6–5 axis. Two of these resemble debris disks: HD 141569 is a transitional disk with no substantial surface density at radii below $\sim$ 95 au (Dent et al. 2005; Jonkheid et al. 2006), and HD 100453 has a CO-based gas mass of only $10^{-4}\,M_\odot$ and an inner cavity of 20 au (Khalafinejad et al. 2015; Collins et al. 2009).

[C I] 1–0: Detections are obtained towards three flaring, group I disks. The detection in HD 100546 shows a clear double-peaked Keplerian profile, while the other two (HD 97048 and Oph IRS 48) are likely contaminated by foreground or extended emission. The upper limits towards HD 163296 and HD 169142 allow both small and large disk models with an ISM-like $[C]/[H]_{gas}$, while the upper limit towards HD 104237 lies between the $R_{\rm c}$ = 10 and 50 au models.

[C I] 2–1: The only detection is towards the very flared and embedded disk, HD 97048. Nearly all the upper limits lie close to, or above, the large ($R_{\rm c}$ = 50 au) disk models with an ISM-like $[C]/[H]_{gas}$. The deepest distance-normalized upper limit is obtained for HD 100453, a gas- or carbon-depleted transitional disk described earlier in this subsection.

[C II] 158 μm: Similarly to CO 6–5, all detections of this line are from group I disks, alhtough contamination cannot be checked as easily as for CO. None of the *Herschel*/PACS [C II] 158 μm upper limits from Meeus et al. (2012); Dent et al. (2013); Fedele et al. (2013b) on our Herbig Ae/Be targets provide strong constraints on the gas content or carbon abundance. Most of the upper limits lie between the fiducial $R_{\rm c}$ = 10 and 50 au models with an ISM-like $[C]/[H]_{gas}$. We have also compared our model grid with the full sample of the above *Herschel* studies (not plotted), and find that the only anomalously deep upper limits are for debris disks, where the gas content is low (e.g., HR 1998, 49 Cet, HD 158352).

Additional comments: HD 50138 may be an evolved star. It was included in the sample as a possible protoplanetary disk and is often treated as such in the literature, but see e.g., Ellerbroek et al. (2015) for a discussion of its unclear nature. Its CO 6–5 upper limit falls between our $R_{\rm c}$ = 10 and 50 au models, while the [C II] detection is an order of magnitude brighter than any of our Herbig Ae/Be disk models.

5.4. Summary of carbon abundance constraints

Our APEX survey observations of the [C I] 1–0 and [C I] 2–1 lines, with typical detection limits within a factor of a few of $10^{-18}\,{\rm W\,m^{-2}}$ at 140 pc, are not yet sensitive enough to strongly constrain $[C]/[H]_{gas}$ in most disks. They require a factor of three to ten improvement. This corresponds to observations of $\approx$10 hours per source with APEX, if overheads are included. Our deep exposures towards HD 100546 and TW Hya demonstrate that detections can be made in this way in the brightest disks. On ALMA, a similar sensitivity can be reached in $\approx$1 h for a synthesized beam of $\approx$0.5″. ALMA is essential for extending the [C I] detection sample beyond the few nearest, brightest disks. Equally importantly, any extended emission around the disk will be filtered out by ALMA. Its spatial resolution is sufficient to resolve the CO snowline and study any associated gas-phase carbon abundance variations in many systems, including TW Hya.

The sensitive detection of [C I] 1–0 towards TW Hya (corresponding to $7 \times 10^{-20}\,{\rm W\,m^{-2}}$ at 140 pc; note that the source is at 55 pc) is consistent with a factor of 100 underabundance of gas-phase carbon, confirming the result of Favre et al. (2013). For HD 100546, the detection ($2 \times 10^{-19}\,{\rm W\,m^{-2}}$ at 140 pc; the source is at 97 pc) suggests a gas-phase abundance close to the interstellar one, consistent with earlier work by Bruderer et al. (2012). For both sources, detailed models of the disk structure, in particular constraining the radial extent of the disk, are needed to determine $[C]/[H]_{gas}$ with better precision. We present such modelling in a companion paper (Kama et al. submitted).

Several sources in our sample have relatively deep upper limits on CO or [C I]. They could be either gas- or carbon-poor. These systems are BP Tau, T Cha, HD 139614, HD 141569, and HD 100453. The latter two have low CO-based gas mass estimates and are often considered debris disk like systems, however without an absolute gas mass determination a carbon depletion cannot be entirely ruled out.

6. Conclusions

We present observations and modelling of the main gas-phase carbon reservoirs in protoplanetary disk atmospheres, C^0 and CO. We observed 37 disks with the APEX telescope, and employed DALI physical-chemical models to interpret the data and investigate the relation of CO, [C I] and [C II] emission with the gas-phase carbon abundance, $[C]/[H]_{gas}$.

1. Among our full sample, CO 6–5 is detected (observed) towards 13 (33) sources; [C I] 1–0 in 6 (12); and [C I] 2–1 in 1 (33). The [C I] detections are extended or of unclear origin in all sources except TW Hya and HD 100546.
2. We detect [C I] 1–0 from the disks around TW Hya and HD 100546, the first unambiguous detections of this line in protoplanetary disks. The HD 100546 emission has a symmetric double-peaked line profile.
3. Based on a grid of models, we find that the survey sensitivity, typically $10^{-19}\,{\rm W\,m^{-2}}$ for [C I] 1–0 and $10^{-18}\,{\rm W\,m^{-2}}$ for [C I] 2–1, needs to be improved by a factor of at least three to obtain useful constraints on $[C]/[H]_{gas}$ for most systems.
4. An underabundance of one order of magnitude for gas-phase carbon cannot easily be masked by other disk properties, if they are known to a level made possible by ALMA, *Herschel*

and *Spitzer* (Fig. 5). Larger underabundances are even more reliably identified. The most essential information for constraining the gas-phase carbon abundance is the radial extent of the gas disk.

5. A comparison with our general grid of models suggests that gas-phase carbon is underabundant by up to a factor 100 in TW Hya, while for HD 100546 the comparison suggests a roughly interstellar abundance. For a detailed analysis, see Kama et al. (submitted).
6. BP Tau, T Cha, HD 139614, HD 141569, and HD 100453 warrant follow-up as potentially carbon-depleted disks.
7. The low detection rate of [C II] emission with *Herschel*/PACS in T Tauri disks is due to insufficient sensitivity, while the Herbig Ae/Be systems with no detection are typically gas-poor debris disks.

Acknowledgements. We thank the anonymous referee for constructive comments which helped to improve the paper, Arnaud Belloche and the APEX staff for assistance during the observations, and Matthijs van der Wiel for discussing his SPIRE observations with us. This work is supported by a Royal Netherlands Academy of Arts and Sciences (KNAW) professor prize, the Netherlands Research School for Astronomy (NOVA), and by the European Union A-ERC grant 291141 CHEMPLAN. A.K. acknowledges support from the Foundation for Polish Science (FNP) and the Polish National Science Center grant 2013/11/N/ST9/00400. R.J.W. is supported by NASA through the Einstein Postdoctoral grant number PF2-130104 awarded by the Chandra X-ray Center, which is operated by the Smithsonian Astrophysical Observatory for NASA under contract NAS8-03060. This publication is based on data acquired with the Atacama Pathfinder Experiment (APEX). APEX is a collaboration between the Max-Planck-Institut für Radioastronomie, the European Southern Observatory, and the Onsala Space Observatory. CHAMP$^+$ was constructed with support from the Netherlands Organization for Scientific Research (NWO), grant 600.063.310.10.

References

Acke, B. & van den Ancker, M. E. 2004, A&A, 426, 151
Andersson, B.-G., Idzi, R., Uomoto, A., et al. 2002, AJ, 124, 2164
Andrews, S. M., Wilner, D. J., Hughes, A. M., Qi, C., & Dullemond, C. P. 2009, ApJ, 700, 1502
Andrews, S. M., Wilner, D. J., Hughes, A. M., Qi, C., & Dullemond, C. P. 2010, ApJ, 723, 1241
Andrews, S. M., Wilner, D. J., Hughes, A. M., et al. 2012, ApJ, 744, 162
Asplund, M., Grevesse, N., Sauval, A. J., & Scott, P. 2009, ARA&A, 47, 481
Bakes, E. L. O. & Tielens, A. G. G. M. 1994, ApJ, 427, 822
Bast, J. E., Brown, J. M., Herczeg, G. J., van Dishoeck, E. F., & Pontoppidan, K. M. 2011, A&A, 527, A119
Bergin, E. A., Cleeves, L. I., Crockett, N., & Blake, G. A. 2014, Faraday Discussions, 168, 61
Bergin, E. A., Cleeves, L. I., Gorti, U., et al. 2013, Nature, 493, 644
Bertout, C., Siess, L., & Cabrit, S. 2007, A&A, 473, L21
Brown, J. M., Herczeg, G. J., Pontoppidan, K. M., & van Dishoeck, E. F. 2012, ApJ, 744, 116
Brown, J. M., Pontoppidan, K. M., van Dishoeck, E. F., et al. 2013, ApJ, 770, 94
Bruderer, S. 2013, A&A, 559, A46
Bruderer, S., van Dishoeck, E. F., Doty, S. D., & Herczeg, G. J. 2012, A&A, 541, A91
Canovas, H., Ménard, F., Hales, A., et al. 2013, A&A, 556, A123
Cardelli, J. A., Meyer, D. M., Jura, M., & Savage, B. D. 1996, ApJ, 467, 334
Carmona, A., van den Ancker, M. E., Henning, T., et al. 2007, A&A, 476, 853
Casassus, S., Hales, A., de Gregorio, I., et al. 2013, A&A, 553, A64
Chapillon, E., Parise, B., Guilloteau, S., Dutrey, A., & Wakelam, V. 2010, A&A, 520, A61
Collins, K. A., Grady, C. A., Hamaguchi, K., et al. 2009, ApJ, 697, 557
Cox, A. W., Grady, C. A., Hammel, H. B., et al. 2013, ApJ, 762, 40
Daemgen, S., Petr-Gotzens, M. G., Correia, S., et al. 2013, A&A, 554, A43
de Gregorio-Monsalvo, I., Ménard, F., Dent, W., et al. 2013, A&A, 557, A133
Dent, W. R. F., Greaves, J. S., & Coulson, I. M. 2005, MNRAS, 359, 663
Dent, W. R. F., Thi, W. F., Kamp, I., et al. 2013, PASP, 125, 477
Di Folco, E., Dutrey, A., Le Bouquin, J.-B., et al. 2014, A&A, 565, L2
Doucet, C., Habart, E., Pantin, E., et al. 2007, A&A, 470, 625
Dutrey, A., Guilloteau, S., & Simon, M. 2003, A&A, 402, 1003
Eisner, J. A., Hillenbrand, L. A., White, R. J., Akeson, R. L., & Sargent, A. I. 2005, ApJ, 623, 952
Ellerbroek, L. E., Benisty, M., Kraus, S., et al. 2015, A&A, 573, A77
Espaillat, C., Calvet, N., D'Alessio, P., et al. 2007, ApJ, 664, L111
Favre, C., Cleeves, L. I., Bergin, E. A., Qi, C., & Blake, G. A. 2013, ApJ, 776, L38
Fedele, D., Bruderer, S., van Dishoeck, E. F., et al. 2013a, A&A, 559, A77
Fedele, D., Bruderer, S., van Dishoeck, E. F., et al. 2013b, ApJ, 776, L3
France, K., Schindhelm, E., Bergin, E. A., Roueff, E., & Abgrall, H. 2014, ApJ, 784, 127
Geers, V. C., Augereau, J.-C., Pontoppidan, K. M., et al. 2006, A&A, 459, 545
Guilloteau, S. & Dutrey, A. 1994, A&A, 291, L23
Guilloteau, S., Dutrey, A., Piétu, V., & Boehler, Y. 2011, A&A, 529, A105
Guilloteau, S., Dutrey, A., & Simon, M. 1999, A&A, 348, 570
Güsten, R., Nyman, L. Å., Schilke, P., et al. 2006, A&A, 454, L13
Habart, E., Natta, A., & Krügel, E. 2004, A&A, 427, 179
Henning, T. & Salama, F. 1998, Science, 282, 2204
Heyminck, S., Kasemann, C., Güsten, R., de Lange, G., & Graf, U. U. 2006, A&A, 454, L21
Howard, C. D., Sandell, G., Vacca, W. D., et al. 2013, ApJ, 776, 21
Huelamo, N., de Gregorio-Monsalvo, I., Macias, E., et al. 2015, ArXiv e-prints
Hussain, G. A. J., Collier Cameron, A., Jardine, M. M., et al. 2009, MNRAS, 398, 189
Isella, A., Natta, A., Wilner, D., Carpenter, J. M., & Testi, L. 2010, ApJ, 725, 1735
Jones, A. 2014, ArXiv e-prints
Jonkheid, B., Kamp, I., Augereau, J.-C., & van Dishoeck, E. F. 2006, A&A, 453, 163
Kamp, I. 2011, in EAS Publications Series, Vol. 46, EAS Publications Series, ed. C. Joblin & A. G. G. M. Tielens, 271–283
Kasemann, C., Güsten, R., Heyminck, S., et al. 2006, in Society of Photo-Optical Instrumentation Engineers (SPIE) Conference Series, Vol. 6275, Society of Photo-Optical Instrumentation Engineers (SPIE) Conference Series, 0
Kastner, J. H., Zuckerman, B., Hily-Blant, P., & Forveille, T. 2008, A&A, 492, 469
Khalafinejad, S., Maaskant, K. M., Marinas, N., & Tielens, A. G. G. M. 2015, ArXiv e-prints
Knude, J. & Hog, E. 1998, A&A, 338, 897
Koerner, D. W. & Sargent, A. I. 1995, AJ, 109, 2138
Lee, J.-E., Bergin, E. A., & Nomura, H. 2010, ApJ, 710, L21
Lodders, K. 2003, ApJ, 591, 1220
Lombardi, M., Lada, C. J., & Alves, J. 2008, A&A, 480, 785
Luhman, K. L. 2001, ApJ, 560, 287
Luhman, K. L. 2004, ApJ, 602, 816
Maaskant, K. M., Honda, M., Waters, L. B. F. M., et al. 2013, A&A, 555, A64
Malfait, K., Bogaert, E., & Waelkens, C. 1998, A&A, 331, 211
Mamajek, E. E. 2008, Astronomische Nachrichten, 329, 10
Matter, A., Labadie, L., Augereau, J.-C., et al. 2015, ArXiv e-prints
Matter, A., Labadie, L., Kreplin, A., et al. 2014, A&A, 561, A26
McCleary, J., Stecklum, B., Grady, C., Woodgate, B., & York, D. 2007, in Bulletin of the American Astronomical Society, Vol. 39, American Astronomical Society Meeting Abstracts, 849
Meeus, G., Montesinos, B., Mendigutía, I., et al. 2012, A&A, 544, A78
Meeus, G., Waters, L. B. F. M., Bouwman, J., et al. 2001, A&A, 365, 476
Miotello, A., Bruderer, S., & van Dishoeck, E. F. 2014, ArXiv e-prints
Monnier, J. D., Tannirkulam, A., Tuthill, P. G., et al. 2008, ApJ, 681, L97
Muders, D., Hafok, H., Wyrowski, F., et al. 2006, A&A, 454, L25
Neuhäuser, R., Sterzik, M. F., Schmitt, J. H. M. M., Wichmann, R., & Krautter, J. 1995, A&A, 297, 391
Panić, O. & Hogerheijde, M. R. 2009, A&A, 508, 707
Panić, O., Hogerheijde, M. R., Wilner, D., & Qi, C. 2008, A&A, 491, 219
Panić, O., Hogerheijde, M. R., Wilner, D., & Qi, C. 2009, A&A, 501, 269
Panić, O., Ratzka, T., Mulders, G. D., et al. 2014, A&A, 562, A101
Panić, O., van Dishoeck, E. F., Hogerheijde, M. R., et al. 2010, A&A, 519, A110
Parvathi, V. S., Sofia, U. J., Murthy, J., & Babu, B. R. S. 2012, ApJ, 760, 36
Pontoppidan, K. M., Blake, G. A., & Smette, A. 2011, ApJ, 733, 84
Pontoppidan, K. M. & Blevins, S. M. 2014, Faraday Discussions, 169, 49
Pontoppidan, K. M., Salyk, C., Bergin, E. A., et al. 2014, Protostars and Planets VI, 363
Preibisch, T., Kraus, S., Driebe, T., van Boekel, R., & Weigelt, G. 2006, A&A, 458, 235
Qi, C., Ho, P. T. P., Wilner, D. J., et al. 2004, ApJ, 616, L11
Rucinski, S. M. & Krautter, J. 1983, A&A, 121, 217
Salyk, C., Pontoppidan, K., Corder, S., et al. 2014, ApJ, 792, 68
Simon, M., Dutrey, A., & Guilloteau, S. 2000, ApJ, 545, 1034
Stark, D. P., Whitney, B. A., Stassun, K., & Wood, K. 2006, ApJ, 649, 900
Thi, W.-F., Mathews, G., Ménard, F., et al. 2010, A&A, 518, L125
Thi, W. F., van Dishoeck, E. F., Blake, G. A., et al. 2001, ApJ, 561, 1074
Thi, W.-F., van Zadelhoff, G.-J., & van Dishoeck, E. F. 2004, A&A, 425, 955
Tielens, A. G. G. M. 2008, ARA&A, 46, 289

Tielens, A. G. G. M. & Hollenbach, D. 1985, The Astrophysical Journal, 291, 722
Tognelli, E., Prada Moroni, P. G., & Degl'Innocenti, S. 2011, A&A, 533, A109
Torres, C. A. O., Quast, G. R., da Silva, L., et al. 2006, A&A, 460, 695
Torres, C. A. O., Quast, G. R., Melo, C. H. F., & Sterzik, M. F. 2008, Young Nearby Loose Associations, ed. B. Reipurth, 757
Torres, R. M., Loinard, L., Mioduszewski, A. J., et al. 2012, ApJ, 747, 18
Torres, R. M., Loinard, L., Mioduszewski, A. J., & Rodríguez, L. F. 2009, ApJ, 698, 242
Tsukagoshi, T., Momose, M., Saito, M., et al. 2015, ArXiv e-prints
Unterborn, C. T., Kabbes, J. E., Pigott, J. S., Reaman, D. M., & Panero, W. R. 2014, ApJ, 793, 124
van Boekel, R., Min, M., Waters, L. B. F. M., et al. 2005, A&A, 437, 189
van der Marel, N., van Dishoeck, E. F., Bruderer, S., et al. 2013, Science, 340, 1199
van der Wiel, M. H. D., Naylor, D. A., Kamp, I., et al. 2014, MNRAS, 444, 3911
van Dishoeck, E. F., Jonkheid, B., & van Hemert, M. C. 2006, Faraday Discussions, 133, 231
van Kempen, T. A., van Dishoeck, E. F., Brinch, C., & Hogerheijde, M. R. 2007, A&A, 461, 983
van Leeuwen, F. 2007, A&A, 474, 653
van Zadelhoff, G.-J., van Dishoeck, E. F., Thi, W.-F., & Blake, G. A. 2001, A&A, 377, 566
Walsh, C., Juhász, A., Pinilla, P., et al. 2014a, ApJ, 791, L6
Walsh, C., Juhász, A., Pinilla, P., et al. 2014b, ApJ, 791, L6
Weinberger, A. J., Becklin, E. E., Schneider, G., et al. 1999, ApJ, 525, L53
White, R. J. & Ghez, A. M. 2001, ApJ, 556, 265
Wichmann, R., Bastian, U., Krautter, J., Jankovics, I., & Rucinski, S. M. 1998, MNRAS, 301, L39
Woodall, J., Agúndez, M., Markwick-Kemper, A. J., & Millar, T. J. 2007, A&A, 466, 1197
Zuckerman, B., Forveille, T., & Kastner, J. H. 1995, Nature, 373, 494

Appendix A: Structure of the disk models

In Figs. A.1 and A.2, we show the density structure and the gas and dust temperature, as well as the ultraviolet field in interstellar units (denoted G_0) for the fiducial T Tauri and Herbig Ae/Be disk models.

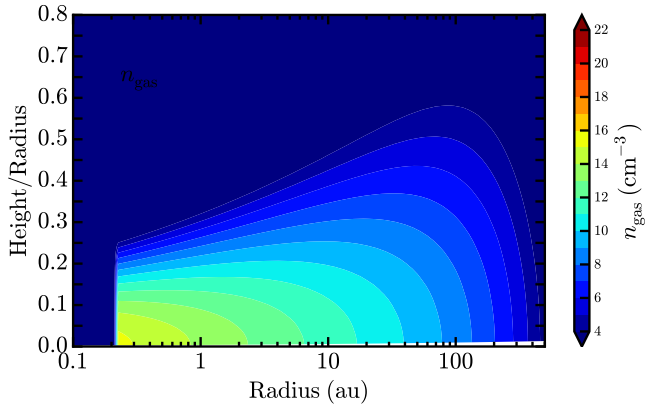

Fig. A.1. The gas density structure of the fiducial disk model.

Appendix B: The degeneracy of [C]/[H]$_{\rm gas}$ with other parameters

The elemental gas-phase carbon abundance ([C]/[H]$_{\rm gas}$). Order-of-magnitude changes in [C]/[H]$_{\rm gas}$ outweigh the impact of reasonable variations of any other individual parameter. The fluxes of all lines except CO 6–5 change by a factor of five for a factor of ten change in [C]/[H]$_{\rm gas}$, implying that large underabundances of the magnitude proposed for TW Hya – more than one order of magnitude – can be reliably identified, if the disk structure is reasonably constrained.

Gas to dust ratio ($\Delta_{\rm gas/dust}$). This parameter is varied by changing the gas mass. Assuming a line becomes optically thick at some fixed column density of gas, and ignoring other effects, the emitting area scales as $A_{\rm em} \propto \Delta_{\rm g/d}^{2/\gamma'}$, where γ' is the the power-law index of the local surface density profile, $\Sigma(r) \propto r^{-\gamma'}$. For the global $\gamma = 1.0$, the CO emission thus scales weakly with the gas mass in the exponentially decreasing outer tail of the surface density (large local γ'). Once the optically thick surface is limited to smaller radii, the relation becomes steeper (small local γ'). The initial slow decrease of the line emission with gas mass is also related to the smaller importance of the cold outer disk, which can be interpreted as a further decline of the surface density of particles in the required upper energy state. For C^0 line fluxes, one order of magnitude in $\Delta_{\rm gas/dust}$ ratio gives the same change as a factor of three in [C]/[H]$_{\rm gas}$. Therefore, an order-of-magnitude scale underabundance of gas-phase carbon can be identified even with a poorly known $\Delta_{\rm gas/dust}$.

The disk surface density power law index (γ). If $\Sigma_{\rm c}$ and $R_{\rm c}$ are fixed, increasing gamma increases the fluxes of all lines. From $\gamma = 0.8$ to 1.5, the C^0 line fluxes can increase by a factor of three to ten. This is related to an increase in disk mass, which doubles. Note that, in the power-law surface density with an exponential taper, $\gamma = 1.5$ yields quite a shallow surface density profile in the exponential tail, which is reflected in an increased CO emitting area in the outer disk.

Disk surface density anchorpoint ($R_{\rm c}$). Given a γ and $\Sigma_{\rm c}$, this parameter sets the radial size of the disk, which can be defined as the extent of optically thick CO emission.

The disk surface density scaling ($\Sigma_{\rm c}(R_{\rm c})$). For a fixed $R_{\rm c}$, this parameter varies the disk mass. For a range of three orders of magnitude in gas mass, the largest line flux variation amplitude (CO 6–5) is a factor of ten.

The flaring parameters (ψ and $h_{\rm c}$). The variation amplitude of ψ leads to up to a factor of five in CO and [C I] line fluxes, but [C II] can vary by an order of magnitude. The CO and C^0 line fluxes depend on ψ in all cases, while C^+ becomes more sensitive with increasing ultraviolet flux (10000 K emission). For a pure 4000 K radiation field, $T_{\rm kin}$ is too low in the tenuous upper layers of the disk to produce substantial [C II] 158 μm emission. Varying $h_{\rm c}$ has up to a factor of two impact on the lines, as it changes the volume of warm gas.

Mass ratio of large to small grains (f). Decreasing the fraction of large grains increases the optical depth of the disk material at short wavelengths, making the emitting regions colder. The ionized carbon is in completely optically thin gas and is less affected. From $f = 0.2$ to 0.999, the variation in CO line flux does not exceed a factor of three, with C^0 and C^+ less affected.

Inner hole size ($r_{\rm hole}$). An inner hole of up to 100 au in size has only a factor of ≤ 2 impact on any of the line fluxes. This parameter is only important if the disk is very small.

List of Objects

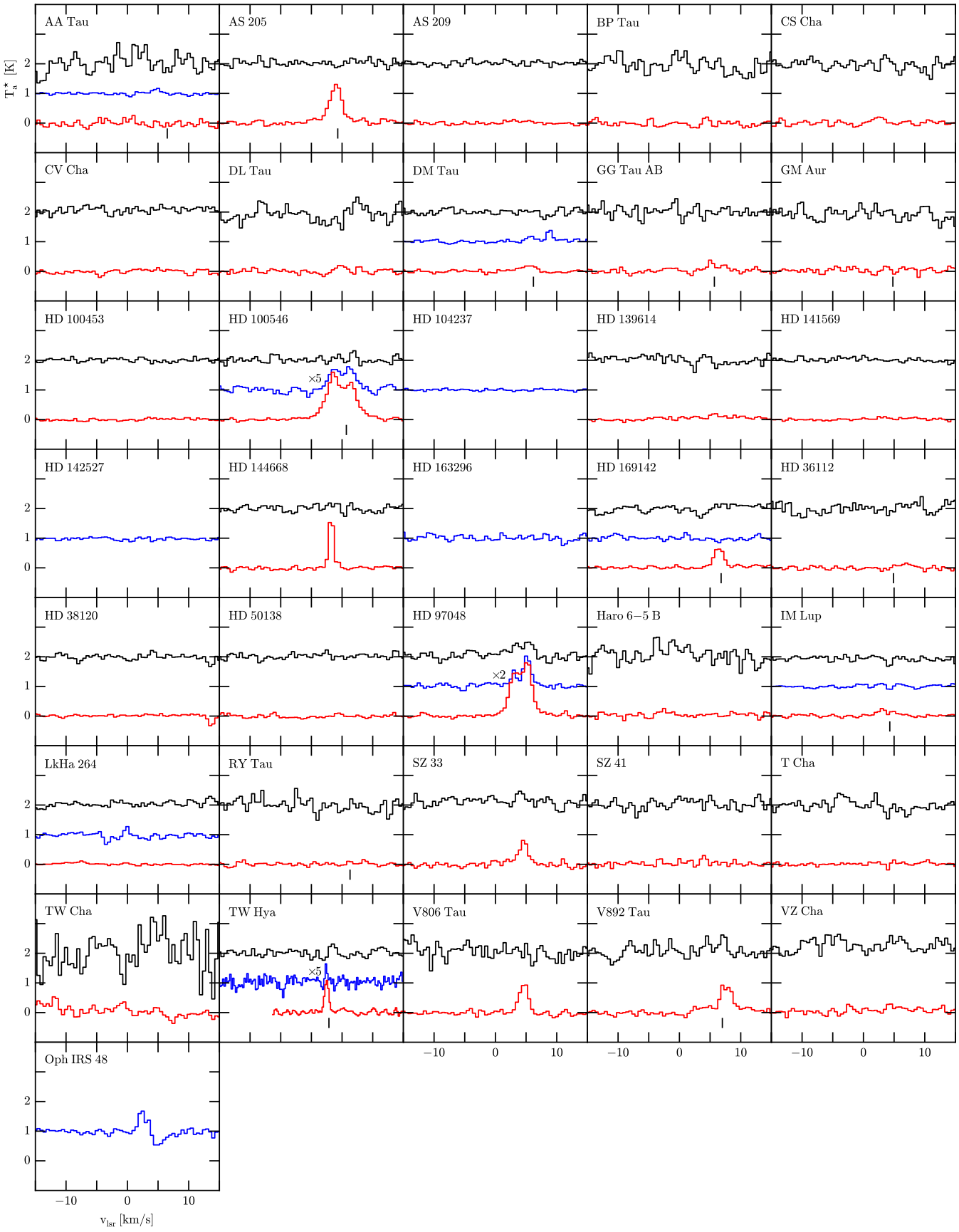

Fig. 2. All observed spectra, rebinned to a resolution of 0.5 km s^{-1}. From bottom to top in each panel, the spectra are CO 6–5 (red), [C I] 1–0 (blue) and [C I] 2–1 (black). The measured fluxes and noise levels are reported in Table 1. Vertical offsets of 1 K have been applied for clarity.

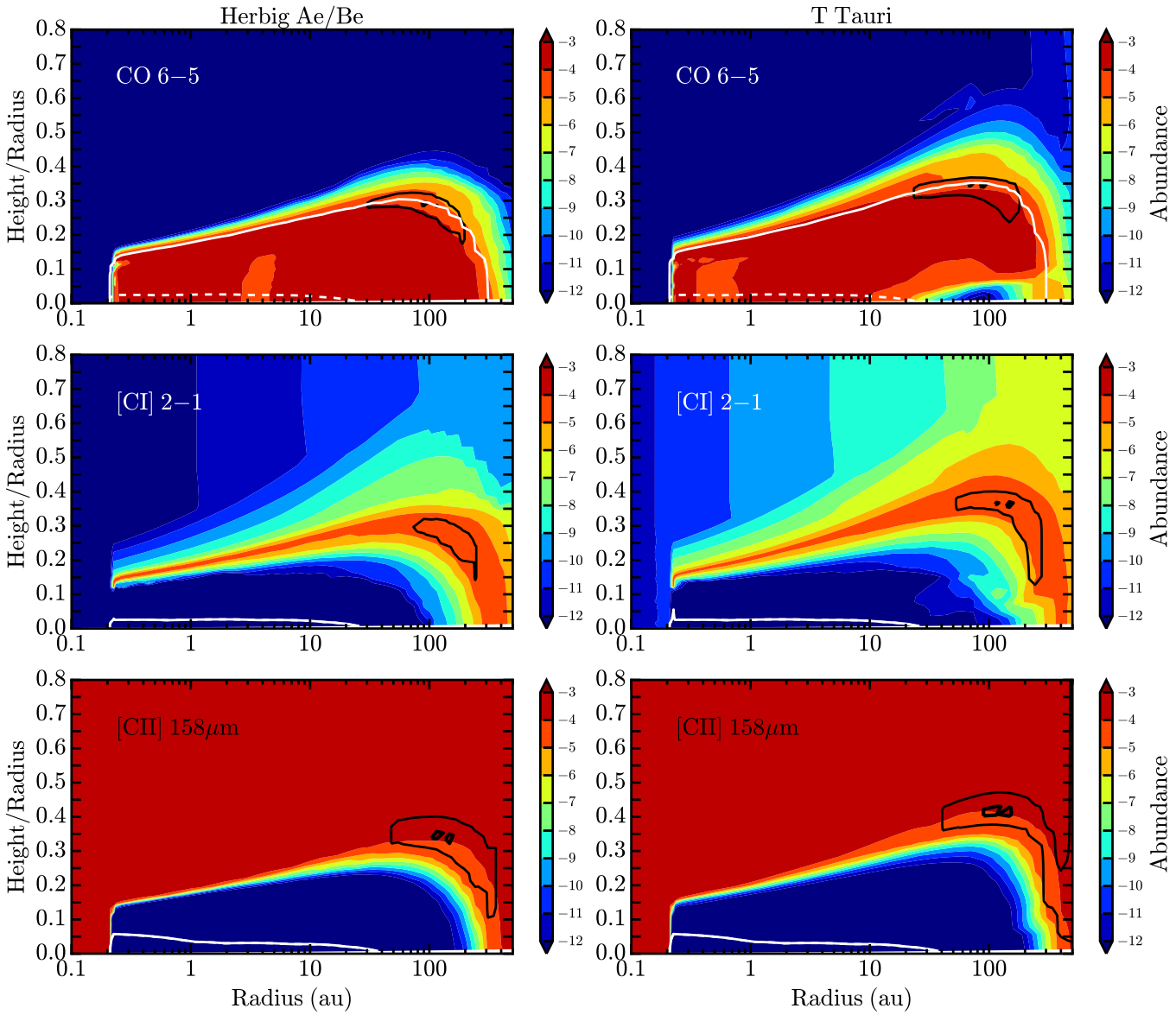

Fig. 4. Maps of the abundance (colour shading) and emission contribution (black lines) of the main gas-phase carbon reservoirs in a disk around a star with $T_{\rm eff}$ = 10000 K (left) and a $T_{\rm eff}$ = 4000 K star with 0.1 $L_\odot$ of UV excess (right). The solid black lines demarkate areas containing 75% (thinner line) and 25% (thicker) of the emission. White lines show the vertical τ = 1 surface for the line (solid) and continuum (dashed) emission.

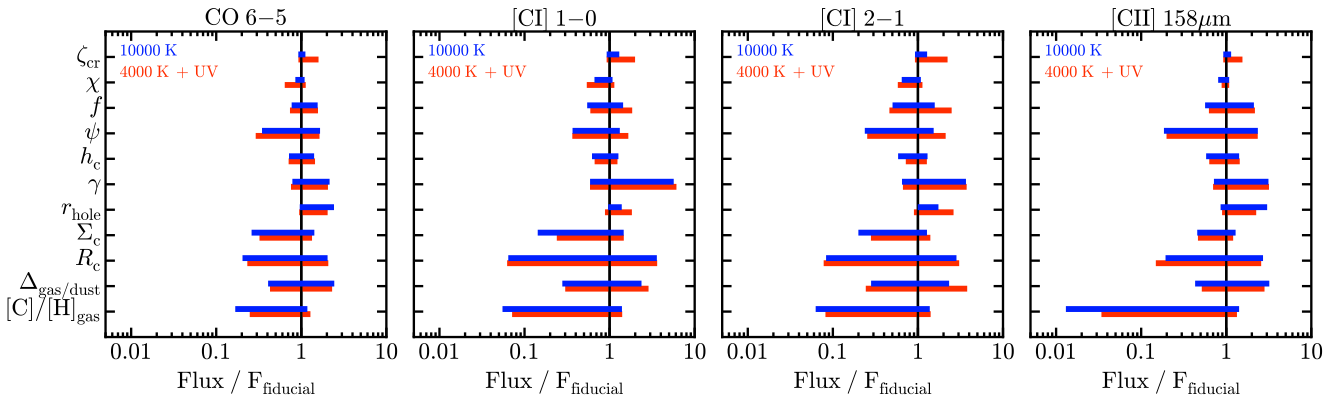

Fig. 5. The effect of model parameter variations on the line fluxes of carbon species in the disk atmosphere. Two central stars are considered: a 4000 K star with UV excess (red), and a pure 10000 K photosphere (blue). Horizontal bars show the range of variation resulting from the parameter values given in Table 4. The fiducial model (black vertical line) is a disk with $R_c = 50$ au and with [C]/[H]$_{gas} = 1.35 \times 10^{-4}$, and the reference fluxes for the 4000 K models are, from left to right, 9.6×10^{-19}, 9.0×10^{-20}, 2.2×10^{-19} and 3.4×10^{-18} W m^{-2}; for 10000 K they are 4.6×10^{-18}, 2.6×10^{-19}, 1.1×10^{-18} and 3.1×10^{-17} W m^{-2}.

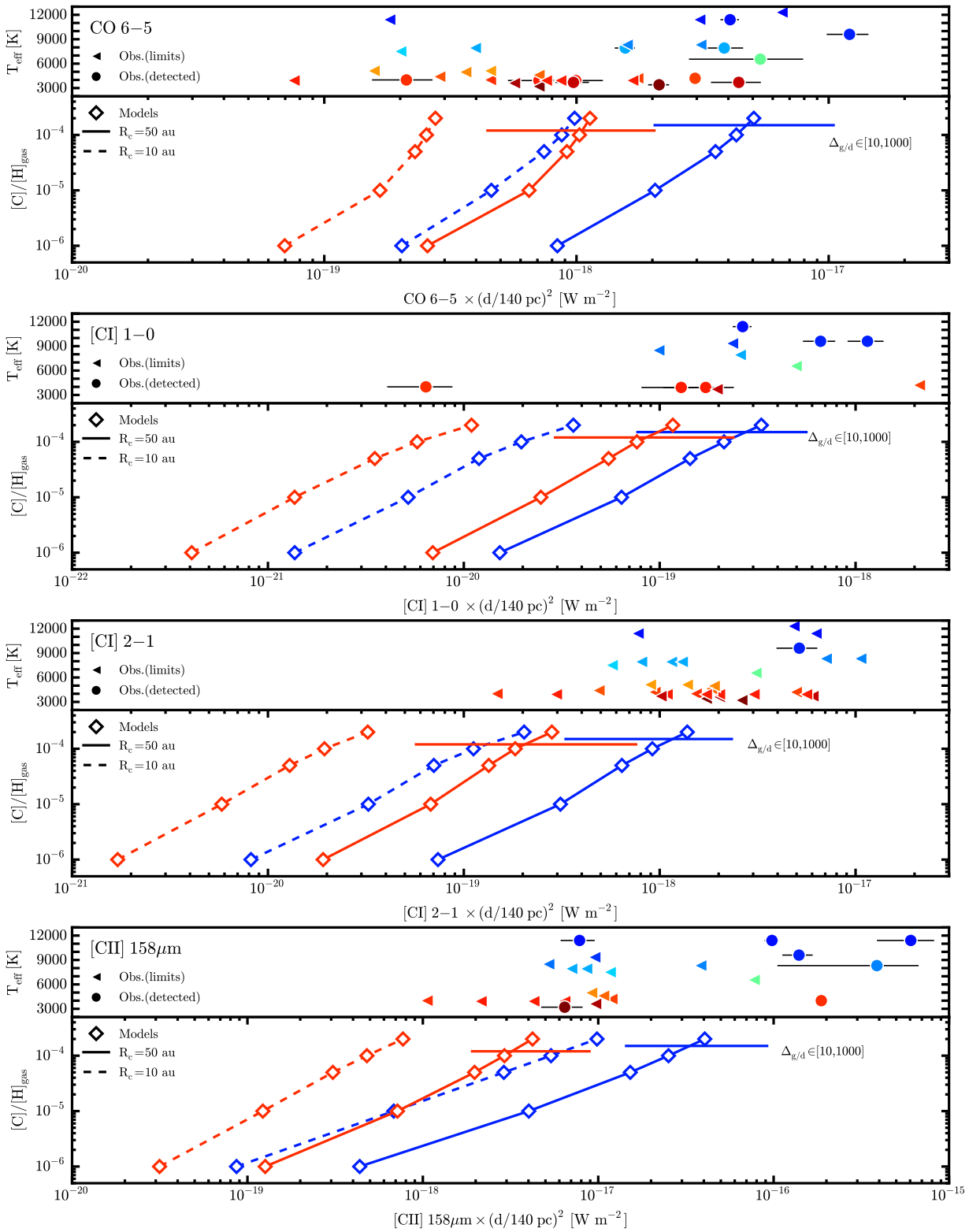

Fig. 6. APEX observations (circles, triangles) and DALI full disk models (diamonds) of the CO 6–5 (top), [C I] 1–0, [C I] 2–1, and [C II] 158 μm (bottom) transitions. All values are colour-coded for the stellar $T_{\rm eff}$, with T Tauri stars red and Herbig Ae/Be stars blue. The fluxes are plotted with stellar $T_{\rm eff}$ values in the upper subpanels (with $[{\rm C}]/[{\rm H}]_{\rm gas} = 1.35 \times 10^{-4}$ and $R_{\rm c} = 50$ au fixed for the fiducial model), and with the gas-phase total elemental carbon abundance, $[{\rm C}]/[{\rm H}]_{\rm gas}$, in the lower subpanels (solid lines connect models with $R_{\rm c} = 50$ au, dashed lines $R_{\rm c} = 10$ au). Horizontal lines in the lower subpanels show the flux changes from varying the gas-to-dust ratio by a factor of ten around the fiducial T Tauri and Herbig Ae/Be models.

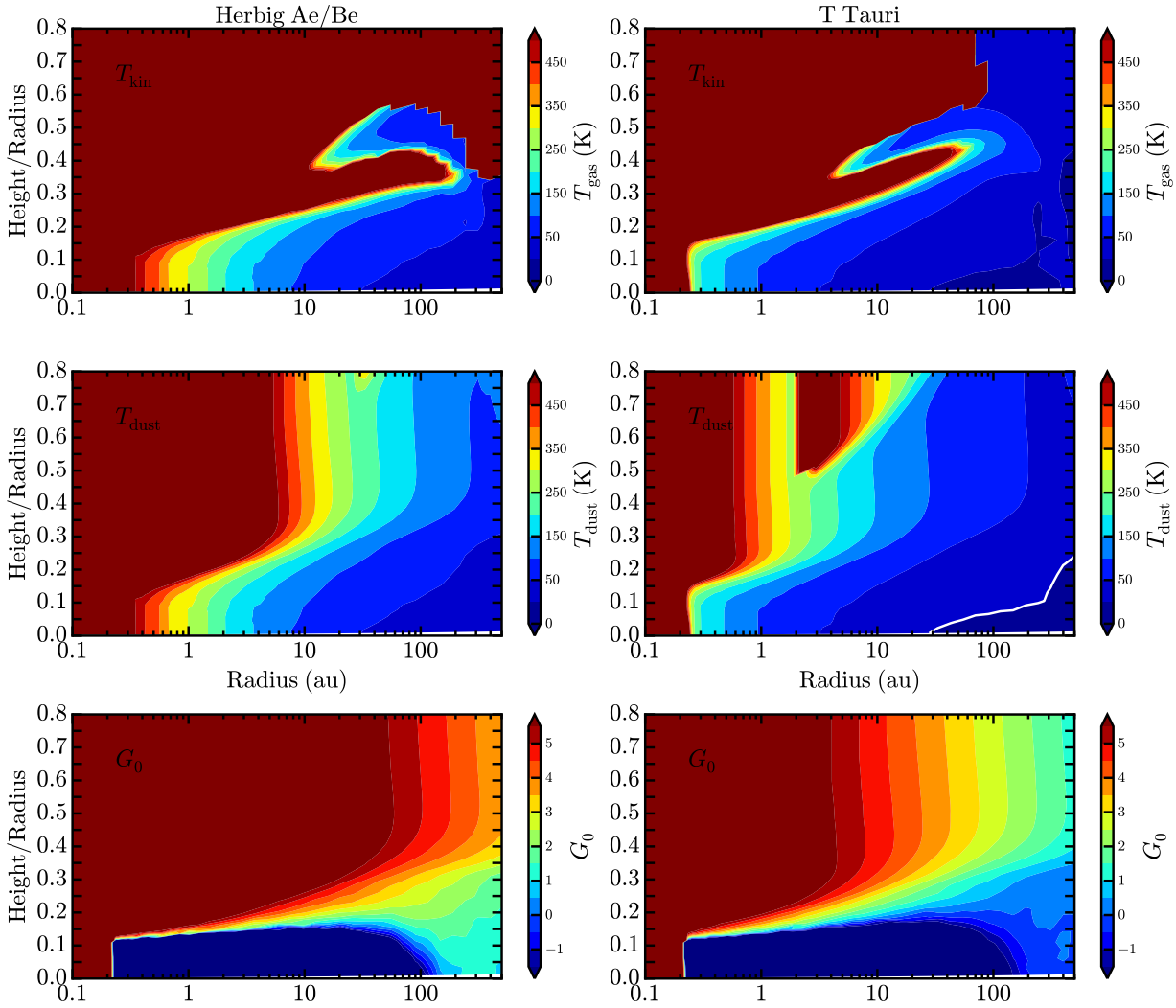

Fig. A.2. The fiducial disk models for a $T_{\rm eff}$ 10000 K star (Herbig Ae/Be, left column) and a $T_{\rm eff}$ 4000 K star with an ultraviolet excess (representing T Tauri disks, right column). From top to bottom, the panels show the gas and dust temperature, and the ultraviolet field in standard interstellar field units, G_0.